Large-Area Ordered Quantum-Dot Monolayers via Phase Separation During Spin-Casting**

By *Seth Coe-Sullivan*, *Jonathan S. Steckel*, *Wing-Keung Woo*, *Moungi G. Bawendi*, and *Vladimir Bulović**

We investigate a new method for forming large-area ($> cm^2$) ordered monolayers of colloidal nanocrystal quantum dots (QDs). The QD thin films are formed in a single step by spin-casting a mixed solution of aromatic organic materials and aliphatically capped QDs. The two different materials phase separate during solvent drying, and for a predefined set of conditions the QDs can assemble into hexagonally close-packed crystalline domains. We demonstrate the robustness and flexibility of this phase-separation process, as well as how the properties of the resulting films can be controlled in a precise and repeatable manner. Solution concentration, solvent ratio, QD size distribution, and QD aspect ratio affect the morphology of the cast thin-film structure. Controlling all of these factors allows the creation of colloidal-crystal domains that are square micrometers in size, containing tens of thousands of individual nanocrystals per grain. Such fabrication of large-area, engineered layers of nanoscale materials brings the beneficial properties of inorganic QDs into the realm of nanotechnology. For example, this technique has already enabled significant improvements in the performance of QD light-emitting devices.

1. Introduction

The colloidal synthesis of inorganic nanocrystal quantum dots (QDs)[1–4] enables tuning of QD material properties with atomic-level precision. Research on devices that harness these properties can be divided into two distinct classes: point-contact devices that utilize a countable number of nanocrystals, or large-area devices that utilize great numbers of QDs. In both cases, controlling the placement of the QDs within the active device structure presents the greatest challenge to device fabrication. Many of the earlier studies dedicated to assembling two-dimensional (2D) and three-dimensional (3D) superlattices of QDs on solid substrates[5–9] present techniques that require long preparation times and precise control of surface interactions to achieve ordered assembly, making the incorporation of such techniques into a working device structure challenging.

The present work investigates the phase separation that occurs during the spin-casting process, which is capable of arranging QDs over large areas (cm^2) in 2D sheets within layered structures. This process simultaneously yields QD monolayers self-assembled into hexagonally close-packed (hcp) arrays and places this monolayer on top of a co-deposited contact. We describe the QD phase-separation and self-assembly processes and how to controllably tune the resulting film properties. The technique has already been used in the structuring of efficient quantum-dot light-emitting devices (QD-LEDs),[10–12] but, as a general and flexible fabrication technique, this method could enable fabrication of a wide variety of large-area nanostructured heterostructures. QD monolayers arranged onto organic thin films are a unique platform for the study of basic physical properties of materials, for example allowing investigation of coarsening mechanisms on the individual adatom (in this case a single-QD) level.[13,14]

The fabrication of a monolayer sheet of close-packed QDs by phase separation during spin-casting is in essence a very simple process, as depicted in Figure 1. The process relies upon the solvation of both the organically capped semiconductor QDs and the organic material to be used as an underlayer in a compatible solvent system. During solvent drying, the QDs phase separate from the organic underlayer material, and rise towards the surface of the film. When drying is complete, the organic material is in the form of a homogenous thin film, which is coated by a layer of QDs. For typical solvent systems, the film is dry well before equilibrium is achieved, and thus the film formation is arrested in a non-equilibrium condition. The exact structure and composition of the layer is completely determined by the composition of the spin-casting solution (for a fixed set of processing conditions). Hence, the material purity of the QD sample is of critical importance to the phase-separation process (see Experimental). As an example, the fabrication can be continued resulting in a complete LED.

While it is impossible for any thin-film fabrication method to be universally applicable, we demonstrate that within the extent of this study, the phase-separation process is not critically

[*] Prof. V. Bulović, S. Coe-Sullivan[+]
Laboratory of Organic Optics and Electronics
Department of Electrical Engineering and Computer Science
Massachusetts Institute of Technology
Cambridge, MA 02139 (USA)
E-mail: bulovic@mit.edu
J. S. Steckel,[+] Dr. W.-K. Woo, Prof. M. G. Bawendi
Department of Chemistry, Massachusetts Institute of Technology
Cambridge, MA 02139 (USA)
[+] These authors contributed equally to this work.

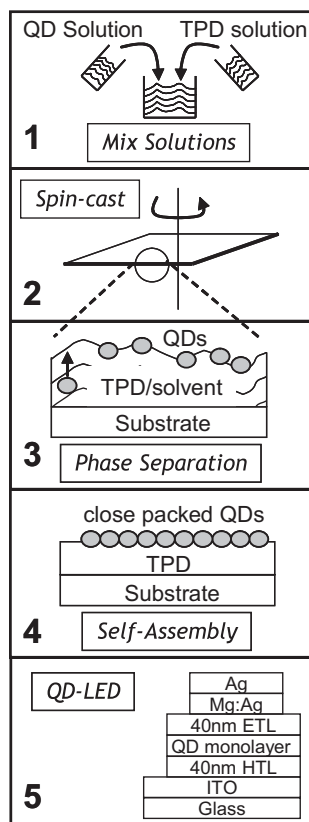 © 2005 WILEY-VCH Verlag GmbH & Co. KGaA, Weinheim **1117**

Figure 1. Graphical description of the fabrication of organic/QD bilayers through phase separation during spin-casting: TPD exemplifies the organic material. The entire process can be completed on the time scale of seconds, differentiating it from other QD self-assembly techniques. This fabrication process enables the creation of efficient QD-LED structures [10], depicted in step 5. ETL: electron-transporting layer; HTL: hole-transporting layer; ITO: indium tin oxide.

Table 1. Examples of materials compatible with the phase-separation process: a list of materials that have been incorporated successfully into the phase-separation process. This list is not meant to be exhaustive, but rather representative of the materials that are compatible. TPD = N,N'-diphenyl-N,N'-bis(3-methylphenyl)-(1,1'-biphenyl)-4,4'-diamine; NPD = 4,4-bis[N-(1-naphthyl)-N-phenylamino]biphenyl; poly-TPD = Poly(N,N'-bis(4-butylphenyl)-N,N'-bis(phenyl)benzidine; CBP = 4,4'-N,N'-dicarbazolyl-biphenyl; Alq$_3$ = tris(8-hydroxyquinoline)aluminum; (CdSe)ZnS = CdSe core/ZnS shell particles; TOPO = Trioctylphosphine oxide; Eponate 12 = trade name of epoxy available from Ted Pella Inc.

Organic hosts	TPD, NPD, poly-TPD, CBP, Alq$_3$, polycarbonate
Solvents	Chloroform, chlorobenzene, toluene, benzene, pyridine
QD core materials	PbSe, CdSe, (CdSe)ZnS, (CdS)ZnS, Au
QD capping materials	Oleic acid, pyridine, TOPO, dodecane thiol
QD core diameter	3–10 nm
QD size aspect ratio	1:1 (spherical), 5:2, 5:1 (nanorod)
Substrates	Silicon, glass, ITO, parylene-C, Eponate 12 epoxy

(N,N'-diphenyl-N,N'-bis(3-methylphenyl)-(1,1'-biphenyl)-4,4'-diamine, an archetypical organic) concentration in the solution is changed from 2 mg mL^{-1} (resulting in 12 nm underlayer film thickness) to 94 mg mL^{-1} (440 nm underlayer film thickness). Figure 2f, inset, shows that the relationship between the TPD concentration in a chloroform solution and the resulting underlayer film thickness is linear. Atomic force microscopy (AFM) images of these surfaces reveal that phase separation is still present in all samples, and that the fraction of QD surface coverage is completely independent of underlayer film thickness. This separation of parameters facilitates optimization of device performance in fabricated structures.

2.2. Control of Monolayer Surface Coverage

The concentration of QDs in the spin-casting solution may also be tuned, with predictable effects on the resulting bilayer. For very low QD concentrations, the bilayer film (see Fig. 2a) contains a countable number of QDs distributed homogeneously on the organic surface. The QDs can be imaged individually, or in close-packed groupings of two or more crystals. As the solution QD concentration is increased, the number of QDs on the surface of the film increases (see Figs. 2b–d). Figure 2f plots the observed percent coverage versus QD concentration in the spin-casting solution.

As the QD solution concentration is increased, a nearly complete coverage of QDs on the organic surface is observed. If the concentration of QDs in the spin-casting solution is further increased, the result is a breakdown of the flat, uniform morphology shown in the other AFM images in this work. As more QDs than can fit try to pack, they are forced to break out of the plane of the monolayer and seek lower-energy conformations. In some cases the QDs pile up into 3D stacks, leaving exposed regions of the organic underlayer. In other cases the first-layer coverage remains high, but a build-up of regions of QD multilayers occurs (Fig. 2e). Within this work we do not study such multilayer structures, but instead focus on the more controllable process of generating ordered monolayer and sub-monolayer coverage.
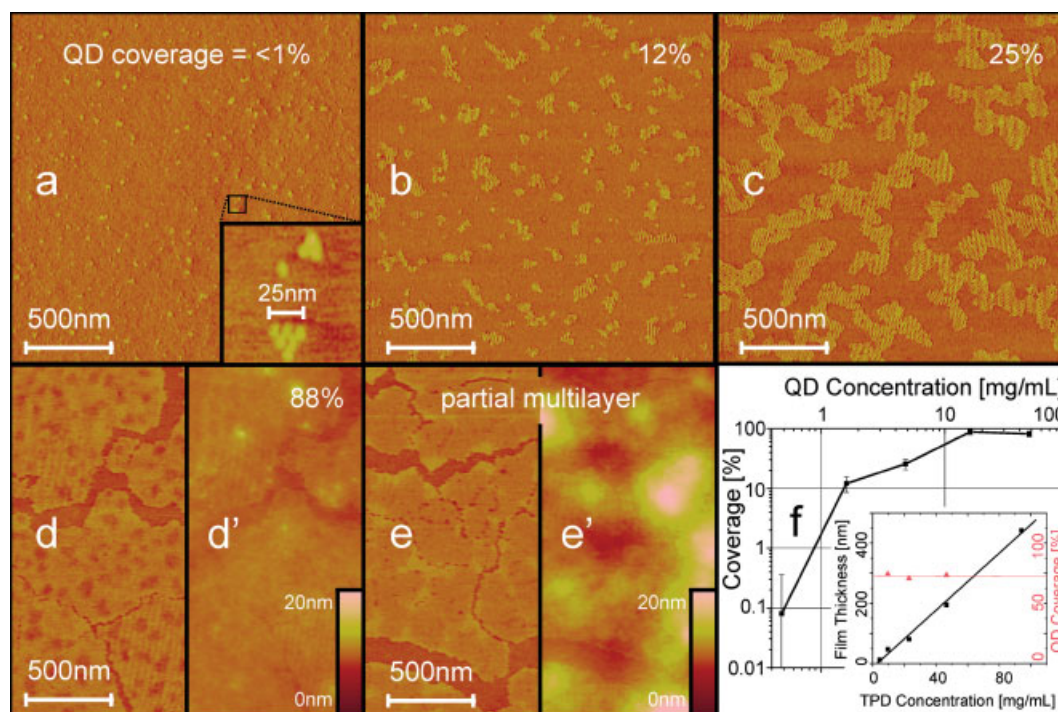
dependant on any one component of the system. We observe phase separation and assembly of QD monolayer sheets for a number of substrates, solvents, organic underlayer materials, QD core materials, QD organic capping groups, QD diameters, QD size aspect ratios, spin-casting parameters, and environmental conditions. Table 1 lists the materials used to demonstrate the generality of this process. The only known constraints on the phase-separation process are 1) that there is a solvent or solvent system which dissolves both QDs and organic materials in the needed concentrations, and 2) that the solvent and organic layer wet the substrate surface.

2. Results and Discussion

2.1. Control of Underlayer Thickness

Perhaps the simplest film property to control in this process is the underlying organic-film thickness. It is well known that the thickness of spin-cast organic thin films may be controlled by varying the solution concentration while fixing the spin parameters. For example, for a fixed set of spin conditions, the phase-separation process remains unaffected when the TPD

Figure 2. Effect of solution concentration on the phase-separation process: Tapping-mode AFM images of QDs assembled on an organic surface. As the concentration of QDs in the spin-casting solution is increased, the surface coverage of QDs is increased. The images show QD partial monolayers (a–d) with various coverages, and a partial multilayer that results from even higher QD solution concentrations (e). a–e) Phase images. d′,e′) The corresponding height images which demonstrate the increase in surface roughness for multilayer QD films. QD concentrations are a) 0.48 mg mL^{-1}, b) 1.6 mg mL^{-1}, c) 4.8 mg mL^{-1}, d) 16 mg mL^{-1}, and e) 48 mg mL^{-1}. f) The dependence of QD monolayer surface coverage on concentration of QDs in the spin-casting solution. Inset: the linear dependence of organic-film thickness on the concentration of organic material in the spin-casting solution (TPD in chloroform). The parameters that are varied in the two plots are completely independent, allowing organic-layer thickness to be tuned independent of QD surface-coverage fraction. The QDs shown here are 6.5 nm-diameter PbSe cores, prepared as described in the Experimental Section.

2.3. Control of Packing Order and Grain Size

2.3.1. Quantum-Dot Size Distribution

The degree of hexagonal packing that is observed on a QD monolayer is directly related to the polydispersity of QD diameter. Figure 3 shows three partial QD monolayers, spin-cast from solutions formulated from three different QD samples. Figure 3a shows an example of a largely disordered film, made from a QD sample with size-distribution standard deviation (σ_{SD}) of >10 %. Although the film stack is determined by the phase-separation process, the self-assembly into
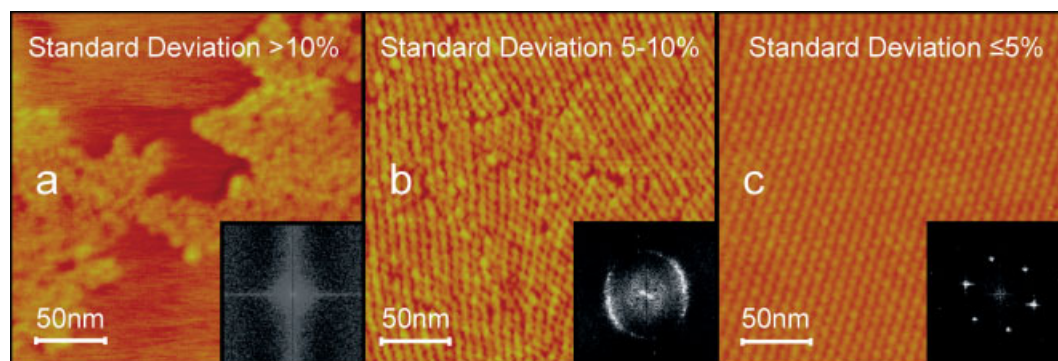

Figure 3. Effect of QD size distribution on the degree of packing order; AFM phase images demonstrating this effect. For broad size distributions (a, CdSe/ZnS core/shell particles (CdSe)ZnS) the QDs assume random packing. As the size distribution is narrowed (b, red-emitting, bare CdSe; c, 5.5 nm PbSe), the QDs clearly pack into hexagonal arrays. For monodisperse samples with $\sigma_{SD} < 5$ % (c), high degrees of order are achievable, with grain sizes larger than 1 µm². Insets: 2D spatial Fourier transforms of the images. For the perfect single grain (c), the Fourier transform reveals the expected six-point pattern. These six points blur into a ring for the image containing a large number of grains (b), and shows no distinct features for the disordered film (a). Fourier analysis is an effective method for measuring the periodicity (QD center-to-center spacing) of the QD monolayers.

an hcp array of particles has been prevented by the size dispersion.

Figure 3b shows a bilayer formed from a QD sample with $\sigma_{SD} = 5$–10%. While it is clear that the QDs have assembled into the hcp monolayer structure, the ordered domains, or grains, remain small, containing at most a few hundred QDs per grain. It is noted that this size distribution is narrow enough to form high-coverage monolayers which are of high enough quality for the fabrication of monochromatic emitting QD-LEDs.

By careful control of QD synthetic techniques, $\sigma_{SD} < 5\%$ is achievable (see Experimental). Figure 3c shows an AFM image of an hcp bilayer created with such a sample, in this case 5.5 nm PbSe QDs with oleic acid caps on a TPD underlayer. The high degree of spatial periodicity of the sample enables clear imaging of individual QDs in the hcp colloidal crystal as depicted in Figure 4. The average grain size exceeds 1 μm², with a high degree of 2D ordering over tens of thousands of repeat units.
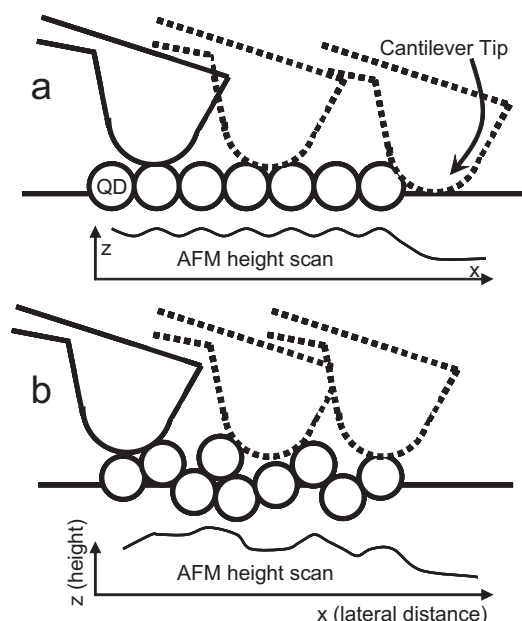

Figure 4. Depiction of the effect of surface roughness on the resolution of AFM. The pervasive use of tapping-mode AFM throughout this work as a primary method of analysis is chosen over other microscopy techniques owing to its ease of use, resolution, and flexibility of substrate compatibility. In contrast, transmission electron microscopy (TEM) requires lengthy preparation techniques that would make the production of optimized devices prohibitive. Also, scanning electron microscopy (SEM) lacks the necessary resolution to easily image individual ~5 nm particles. The AFM image resolution is in part determined by the probe-tip radius, which was specified as <10 nm for all the probes used for this work. The ability to resolve features that are smaller than this tip radius is due to the flatness of the samples (as in Fig. 4a). For exceptionally flat samples, imaging is done with the extreme tip of the probe, whereas the presence of any larger height variations (as when surface disorder is present) results in imaging with the entire tip diameter, setting the minimum resolvable feature size to ~20 nm (as in Fig. 4b). Smooth surfaces allow for resolution below the size scale of the probe-tip diameter.

2.3.2. Quantum-Dot Size Aspect Ratio

QD eccentricity, or size aspect ratio, also determines the degree of self-assembled order in these QDs monolayers.[15] Many of the II–VI colloidal semiconductors have a wurtzite crystal structure, with a unique c-axis in the crystal unit cell. Recent work has exploited this asymmetry in the crystal structure to create growth anisotropy, yielding nanocrystals with controllably tuned size eccentricity from $R_A = 1.0$ (spherical) to several 100 (rod-shaped nanocrystals).[4] Figure 5 demonstrates that the phase-separation process is unaffected by changes in aspect ratio from $R_A = 1$ to 5, but that the degree of ordering is reduced in samples made from more rod-like nanocrystals. In these nanorod monolayers the minimum-energy phase is likely liquid-crystalline rather than the hcp structure we see for $R_A = 1$ nanocrystals.

2.4. Effect of Solvent

The crystallinity of the ordered domains is strongly affected by the solvent drying time during the spin-casting process. Solvent drying time is directly related to solvent-vapor pressure, and a wide range of control is possible using only two miscible solvents. We chose to work with chloroform and chlorobenzene, as they have similar solubility properties (both solvate TPD and oleic acid-capped QDs effectively), but very different vapor pressures (chloroform: 26.2 kPa, chlorobenzene: 1.6 kPa). Chloroform solutions dry in less than a second during the spin-coating process, while chlorobenzene solutions dry only after several seconds of spinning. A continuous range of solvent drying times could be achieved by mixing these two solvents in different ratios.

The equilibrium condition for monodisperse ($\sigma_{SD} < 5\%$) QDs arranged into a 2D sheet is a single hcp grain. A trend towards equilibrium is demonstrated in Figure 6, which depicts a series of spin-cast bilayer films that are made from the same QD sample and the same concentrations of both QDs and TPD. The solvent used is varied from 100% chloroform (fastest drying, Figs. 6a,d) to 100% chlorobenzene (slowest drying, Figs. 6c,f). The mean QD island size is maximized for the mixed-solvent system. Small grain boundaries, however, are visible in the 8 μm scan (Fig. 6e) and are more clearly visible in the 2 μm scan (Fig. 6b) of the mixed-solvent sample. Such grain boundaries, internal to an island, do not occur in the chlorobenzene sample, where almost every island is a single grain, in many cases larger than 1 μm².

Cracking between the large-area islands is likely a result of the solvent drying process, as the optimal particle spacing for solvated QDs differs from the dry QD spacing.[16] In Figure 6d the cracks are of nearly fixed width, suggesting that adjacent islands were once joined together. While solvent is still surrounding the QDs during the spin-casting process, they pack into hcp arrays with some natural period corresponding to the spacing of solvent-rich QDs. At this stage, the surface coverage is probably very close to 100%, and the QDs have some freedom to minimize their surface free energy. As the solvent con-
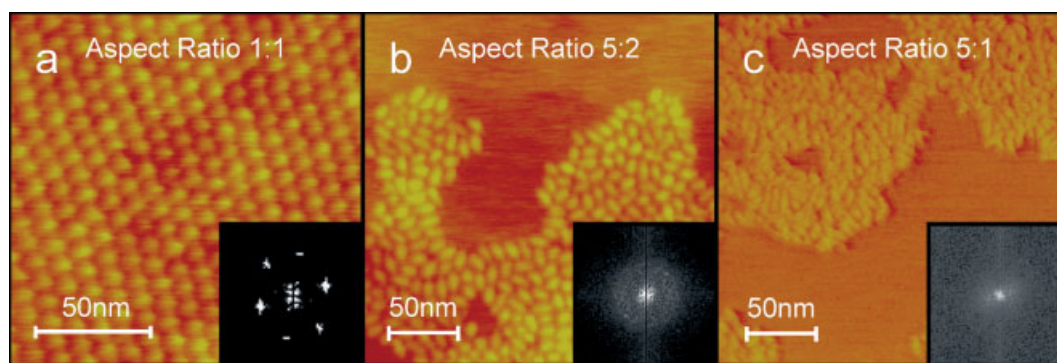
Figure 5. AFM images depicting the effect of QD diameter aspect ratio on degree of ordering. For spheres with narrow size distributions the packing is highly ordered (a), while for samples with larger aspect ratios (b,c) packing is observed but ordering is non-existent. This is due in part to the lack of size monodispersity on the length of the QDs, which is independent of the diameter monodispersity in these samples. Insets: the spatial Fourier transform of the images, highlighting the differences in order between the images. The nanocrystals used in this study are a) 7 nm PbSe QDs, b) red-emitting CdSe core/shell QDs, and c) CdSe nanorods.
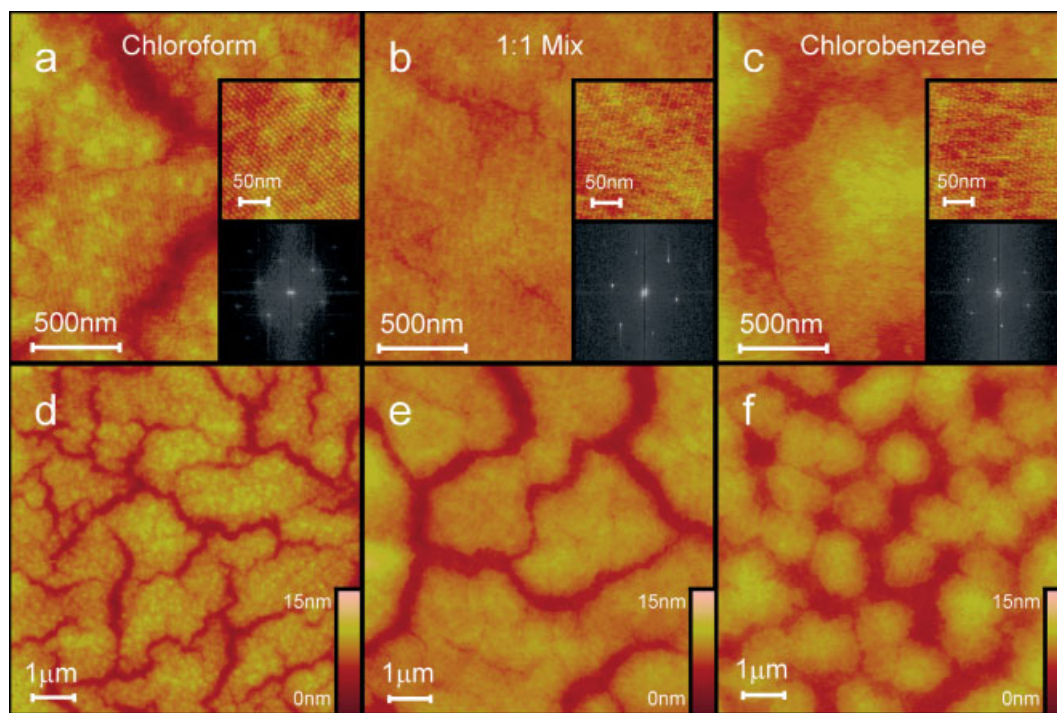

Figure 6. Effect of solvent on grain size and structure: AFM height images of QD monolayers on TPD spun from identical concentration solutions of different solvents. a,d) Images of the same film spun from chloroform at different scan sizes, b,e) images of the same film spun from a 1:1 chloroform/chlorobenzene mixture at different scan sizes, and c,f) images of the same film spun from chlorobenzene at different scan sizes. In (f) each island is a single grain of colloidal crystal (sizes exceeding 1 μm^2), while in (d) and (e) the islands are composed of multiple grains separated by narrow grain boundaries that are observable in images (a) and (b), respectively. The insets in (a–c) are close-up views of the individual QDs that make up the hcp grains, as well as spatial Fourier-transform images showing the hexagonal periodicity of the QD self-assembled monolayers. The QDs shown here are 6.5 nm diameter PbSe cores, prepared as described in the Experimental Section.

tinues to evaporate, the QD spacing decreases, and the QDs in a given grain pack closer together. At some point the continuous QD layer must break to allow for the strain that results from this higher packing density. The breaking is most likely to occur at a grain boundary, as the van der Waals interactions that are holding the QDs to their neighbors are weakest at this point of the film. The result is the large-scale cracking mor-

phology that we observe in Figure 6d, with the perimeters of adjacent islands tracking each other almost perfectly.

For quickly drying solvents, the cracks seem to be more numerous, but smaller in width, while for slowly drying solvents the cracks are less frequent, but larger. In all cases, the total area of void is approximately constant (22 %, 20 %, and 27 % respectively for chloroform, mixed, and chlorobenzene solu-

tions). This implies that the QDs are packing into their equilibrium, dry packing distance in all situations, an effect confirmed by directly measuring the QD spacing on the AFM images (periods of 8.3, 8.1, and 8.3 nm were observed, respectively, for chloroform, mixed, and chlorobenzene solutions). The tendency for slower-drying solvents to yield larger cracks could be due to several factors. First, there are fewer grain boundaries available in this system, because of the larger mean grain size, and thus fewer sites where a crack could originate. The shrinking process is also occurring much more slowly in these films, allowing more time for the strain induced by shrinking to propagate to an existing crack, rather than nucleate a new one. Alternatively, the cracking could occur at many sites very early in the drying process, with the slower drying times allowing more time for the cracks to heal, and for islands to coalesce.

2.5. Observation of Two-Dimensional Crystal Defects

The creation of large-area 2D super-lattices of nanocrystals allows the direct observation of colloidal-crystal defects. There are of course fundamental differences between this colloidal-crystal system and a single-crystalline semiconductor, or a molecular crystal. The size scale is larger, and therefore single elements of the crystal are more easily observed. In addition, we can tune this critical size by growing larger particles. Another major difference is that all of the units are not identical, with slightly different sizes, aspect ratios, and surface chemistry all affecting the process of crystallization. Finally, the energies involved are vastly different, with only van der Waals interactions playing a role. Crystal formation in the plane of a substrate in van der Waals-bonded solids is not completely understood, indicating a potential benefit in using this system to study the kinetics of crystallization.

Figure 7 highlights crystal defects found in a QD self-assembled grain on an organic underlayer. Vacancies are manifested as dark spots in the AFM image of the hcp array (Fig. 7a). Interstitial defects are imaged as a rare high spot in the AFM height scan, roughly one QD diameter higher than the remainder of the periodic pattern. Line defects, where two rows of QDs merge and become one row, are frequently observed (Fig. 7a). Finally, the fine structure of the grain boundary itself is observable (Fig. 7b). It is simultaneously possible to measure the grain angle deviation of two grains joining, and to identify the location of each QD that makes up the boundary.

2.6. Role of Organic Underlayer

Drying-mediated phase-separation and self-assembly processes have recently received much attention in the literature,[6,17,18] though a detailed mechanism for the specific cases presented in this study are as yet unproven. During spin-casting, the organic-material/QD solution undergoes a transition from a homogeneous liquid mixture to a phase-separated solid.
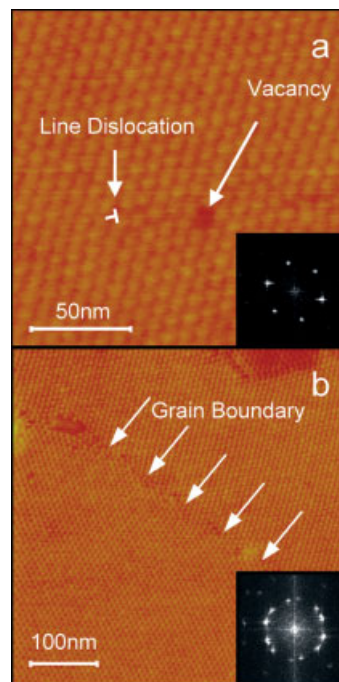

Figure 7. Crystal defects in 2D QD colloidal crystals: AFM images of a) a single QD grain, with crystal defect points clearly visible and b) the grain boundary between two large-area colloidal-crystal grains, allowing the study of the individual QDs that make up the grain edges. Insets: the spatial Fourier transforms of the two images, in (a) showing the three-fold symmetry (six points) of the hexagonal periodic array, and in (b) showing the six points of each of the two grains, resulting in twelve clearly distinguishable points on the same-diameter circle. The QDs shown here are 5.5 nm diameter PbSe cores, synthesized as described in the Experimental Section.

It is unclear at exactly what point in time the separation occurs: a) early in the solvent drying, when the solute mass percent remains low, or b) late in the process, when the solvent mass percent is low. The phase separation is driven by the minimization of interface surface energies. The organic small molecules are preferentially deposited on the substrate surface owing to both their higher polarizability relative to QDs, and the higher contact area with a flat surface which they can achieve. The size of the QD units reduces both of these quantities relative to the small molecules.

Experiments in which the organic component has been eliminated from the spin-casting solution demonstrate that one of the roles of the organic component is a simple surface modification; Neat QD solutions spun onto aromatic organic surfaces form monolayer films with hcp structure, while QD solutions spun onto silicon oxide form low-coverage multilayers or sub-monolayers.[19] Another important effect of the organic material is to slow down the evaporation of the solvent, allowing more time for the QDs to reach equilibrium on the surface. It is the combination of these two effects of the organic material that enable the monolayer formation and self-assembly to occur during the solvent drying time. Once phase separation has occurred, the QDs are mobile on the organic underlayer surface,[13,20] and self-assemble into hcp arrays as they seek their equilibrium conformation, coarsening via a combination of

Ostwald ripening[21,22] and cluster diffusion,[23] depending on the stage of coarsening and the initial QD concentration.

2.7. Light-Emitting Devices

Figure 8 demonstrates the highest external quantum efficiency, $\eta_{EX} > 2\%$, QD-LED created to date. The layered device structure (Fig. 8a, lower inset) requires the use of a QD monolayer, which in this case is created using the phase-separation technique. Holes and electrons are efficiently delivered to the active layers of the device to create excitons which recombine in the cores of the QDs. The electroluminescence (EL) spectrum (Fig. 8b, inset) demonstrates that the emission is dominated by QD band-edge emission. Such a device is reported here to demonstrate both the utility of this fabrication technique, and the need for precise control of all aspects of the process, leaving device analysis for other works.[11] In such a device

the underlayer becomes the hole-transport layer, and the monolayer surface coverage and size distribution of the QD sample are directly related to the EL emission spectrum. The ability to use the phase-separation technique on diverse substrates allows an indium tin oxide (ITO) transparent electrode to be one contact of the device.

3. Conclusion

The fabrication of QD/organic bilayers via phase separation during spin-casting is a robust and general process. It has already been shown to be a useful technique for the creation of new optoelectronic device structures, enabling the creation of high-efficiency QD-LEDs. In addition to the creation of single monolayers of QDs on top of organic semiconductor contacts, this process enables the creation and study of large-scale hcp crystal (super-lattice) domains of only two dimensions, which may be fabricated in seconds. The size scale of these domains is controllable, with a demonstrated maximum grain size in excess of a square micrometer. The upper limit of the grain sizes that could be formed certainly has not yet been reached. The facile assembly of large-area arrays of nanoscale active elements, enabling the creation of macroscale devices from nanoscale materials, is an essential step to transforming nanoscience into nanotechnology.

4. Experimental

Phase Separation: A known quantity of the organic material is weighed out dry, solvated in the chosen solvent, and stirred until completely dissolved. Some quantity of QD solution is then added, to yield both the desired organic-to-QD ratio, as well as overall concentration of solution. For example, in the bilayers used in Figure 4a, the final solution contained 10 mg mL^{-1} of N,N'-diphenyl-N,N'-bis(3-methylphenyl)-(1,1'-biphenyl)-4,4'-diamine (TPD), and 9 mg mL^{-1} of QD sample solid dissolved in chloroform. For simplicity and reproducibility all of the QDs are handled as stock solutions. The final concentration of particles in the spin-casting solution is determined by accurately measuring out a volume of this QD stock into the already prepared solution of organic small molecules. This mixture is then spin-cast onto a substrate. The entire substrate surface must be wetted by the solution before spin-casting begins. The separation process is observed for a wide range of spin-casting parameters such as speed, acceleration, spinning time, and atmosphere (gas, temperature, and solvent content). For the best control and consistent reproducibility of bilayers, we use a single spin speed (3000 rpm (rpm: revolutions per minute)), a maximum starting acceleration (10 000 rpm s^{-1}), and a long spinning time (60 s) to ensure complete evaporation of all solvent. Film properties can then be tuned by changing the solution composition.

Quantum-Dot Clean-up Procedure: The QD growth solution is purified by solvent precipitation twice before spin-casting. A typical procedure is to: a) crash the QDs out of growth solution using an incompatible solvent, b) centrifuge the mixture, c) pour off the supernatant, d) rinse the crystals with an incompatible solvent, e) redisperse the crystals in a compatible solvent, f) crash the crystals out with incompatible solvent, g) centrifuge the mixture, h) decant the supernatant, i) rinse the crystals with an incompatible solvent, j) decant the supernatant, k) redissolve the crystals in a compatible solvent, l) filter the solution, m) remove the solvent using vacuum until the crystals are completely dry, and n) redisperse the crystals in the spin-casting solvent to make a stock solution.
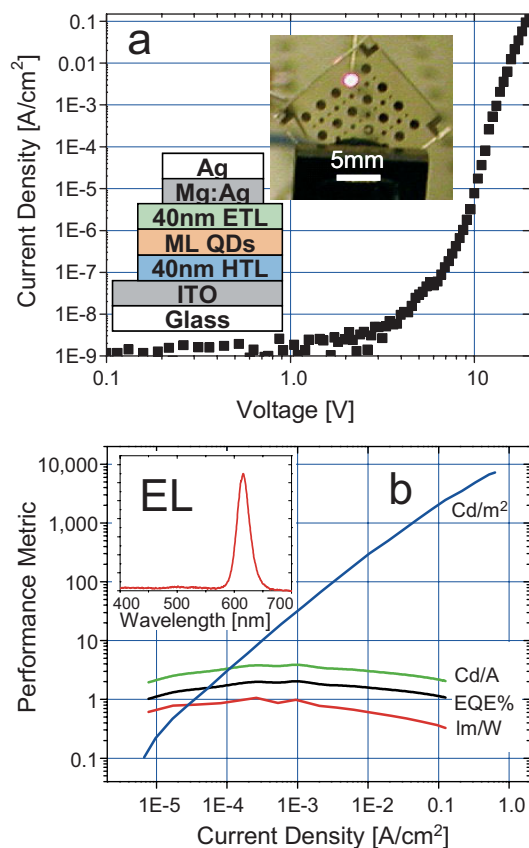

Figure 8. Structure and performance of a QD-LED fabricated using the phase-separation-during-spin-casting method. a) Current–voltage characteristics of the device; lower inset: typical cross-section of an efficient QD light-emitting diode; and upper inset: a photo of the operating 1 mm-diameter device. ETL: electron-transporting layer; ML: monolayer; HTL: hole-transporting layer; ITO: indium tin oxide. b) Critical performance metrics of the QD-LED, with external quantum efficiency in excess of 2 %, > 1 lm W^{-1}, and a maximum brightness of over 7000 Cd m^{-2}; inset: EL spectrum of the QD-LED, with saturated-color red emission peaking at 615 nm, and full width at half maximum of 27 nm. This device used CdSe/ZnS core–shell QDs provided by Quantum Dot Corporation.

Monodisperse PbSe Quantum-Dot Synthesis: A solution of 1 mmol of lead acetate trihydrate (Aldrich, 99.99 %) and 2 mmol of oleic acid (TCI America, 99 %) in 12 mL of trioctylphosine (TCI America, run once through a column of basic activated aluminum oxide) is degassed for 2 h at 300–500 mtorr and 100–120 °C. 5 mL of 1 M trioctylphospine selenide is injected at 140 °C and grown for 4.5 min while the temperature is ramped back up to ∼140 °C. After the growth time, the heating mantle is removed, allowing the solution to cool to room temperature. See Figure 9 for the absorption and emission spectra of such a QD preparation.
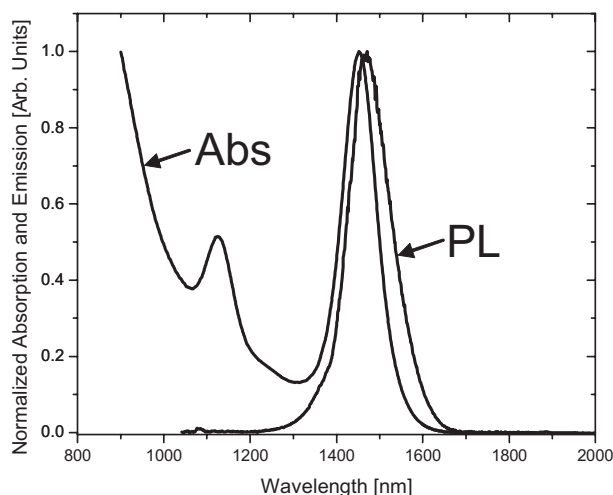

Figure 9. Absorption and photoluminescence (PL) emission spectra of a typical PbSe oleic acid-capped QD sample (core diameter is 5.0 nm in this example) prepared by the route detailed in the Experimental section. The PL full width at half of maximum is 115 nm (66 meV), peaking at wavelength $L = 1470$ nm. The first absorption feature peaks at $L = 1452$ nm.

Optical absorption spectra of PbSe QDs dispersed in trichlorotrifluoroethane were taken on a Carry 5E, (ultraviolet visible near infrared) UV-Vis-NIR spectrophotometer. NIR photoluminescence spectra of PbSe QD solutions were acquired using an InGaAs photodiode array cooled to 173 K (Roper Scientific OMA V) and monochromator. The atomic force micrographs were taken using a Veeco Metrology Dimension 3000 stage with a Nanoscope 3 A controller. QD-LED electroluminescence spectra were acquired with an Ocean Optics USB2000 Miniature Fiber Optic Spectrometer, while the QD-LED was turned on using a Tektronix 577 curve tracer. The current-voltage measurements and external quantum efficiency measurements were performed with a Hewlett Packard 4145B Semiconductor Parameter Analyzer and a Newport silicon photodiode (Model 818-UV) interfaced using LabView.

[1] C. B. Murray, D. J. Norris, M. G. Bawendi, *J. Am. Chem. Soc.* **1993**, *115*, 8706.
[2] B. O. Dabbousi, J. Rodriguez Viejo, F. V. Mikulec, J. R. Heine, H. Mattoussi, R. Ober, K. F. Jensen, M. G. Bawendi, *J. Phys. Chem. B* **1997**, *101*, 9463.
[3] M. A. Hines, P. Guyot-Sionnest, *J. Phys. Chem.* **1996**, *100*, 468.
[4] L. Manna, E. C. Scher, A. P. Alivisatos, *J. Am. Chem. Soc.* **2000**, *122*, 12 700.
[5] C. B. Murray, C. R. Kagan, M. G. Bawendi, *Science* **1995**, *270*, 1335.
[6] X. M. Lin, H. M. Jaeger, C. M. Sorensen, K. J. Klabunde, *J. Phys. Chem. B* **2001**, *105*, 3353.
[7] V. Santhanam, R. P. Andres, *Nano Lett.* **2004**, *4*, 41.
[8] B. O. Dabbousi, C. B. Murray, M. F. Rubner, M. G. Bawendi, *Chem. Mater.* **1994**, *6*, 216.
[9] C. P. Collier, R. J. Saykally, J. J. Shiang, S. E. Henrichs, J. R. Heath, *Science* **1997**, *277*, 1978.
[10] S. Coe, W. K. Woo, M. Bawendi, V. Bulovic, *Nature* **2002**, *420*, 800.
[11] S. Coe-Sullivan, W. K. Woo, J. S. Steckel, M. Bawendi, V. Bulovic, *Org. Electron.* **2003**, *4*, 123.
[12] J. S. Steckel, S. Coe-Sullivan, V. Bulovic, M. G. Bawendi, *Adv. Mater.* **2003**, *15*, 1862.
[13] J. Tang, G. L. Ge, L. E. Brus, *J. Phys. Chem. B* **2002**, *106*, 5653.
[14] A. Lo, R. T. Skodje, *J. Chem. Phys.* **2000**, *112*, 1966.
[15] N. R. Jana, *Angew. Chem. Int. Ed.* **2004**, *43*, 1536.
[16] S. Connolly, S. Fullam, B. Korgel, D. Fitzmaurice, *J. Am. Chem. Soc.* **1998**, *120*, 2969.
[17] E. Rabani, D. R. Reichman, P. L. Geissler, L. E. Brus, *Nature* **2003**, *426*, 271.
[18] H. Tanaka, *J. Phys. Condens. Matter* **2000**, *12*, R207.
[19] M. Maillard, L. Motte, M. P. Pileni, *Adv. Mater.* **2001**, *13*, 200.
[20] B. A. Korgel, D. Fitzmaurice, *Phys. Rev. Lett.* **1998**, *80*, 3531.
[21] K. Morgenstern, G. Rosenfeld, G. Comsa, *Phys. Rev. Lett.* **1996**, *76*, 2113.
[22] J. M. Wen, J. W. Evans, M. C. Bartelt, J. W. Burnett, P. A. Thiel, *Phys. Rev. Lett.* **1996**, *76*, 652.
[23] G. L. Ge, L. E. Brus, *Nano Lett.* **2001**, *1*, 219.